Journal of Solid State Chemistry 181 (2008) 1816–1823

Contents lists available at ScienceDirect

Journal of Solid State Chemistry

journal homepage: www.elsevier.com/locate/jssc

On the microstructure and symmetry of apparently hexagonal $BaAl_2O_4$

A.-K. Larsson [a,*], R.L. Withers [a], J.M. Perez-Mato [b], J.D. Fitz Gerald [c], P.J. Saines [d], B.J. Kennedy [d], Y. Liu [a]

[a] Research School of Chemistry, Australian National University, Science Road, Canberra ACT 0200, Australia
[b] Department of Condensed Matter Physics, University of the Basque Country, Bilbao, Spain
[c] Research School of Earth Sciences, Australian National University, Canberra ACT 0200, Australia
[d] School of Chemistry, University of Sydney, Sydney NSW 2006, Australia

ARTICLE INFO

Article history:
Received 18 December 2007
Received in revised form
1 March 2008
Accepted 30 March 2008
Available online 20 May 2008

Keywords:
$BaAl_2O_4$
Crystal structure
TEM
Neutron diffraction
Symmetry

ABSTRACT

The $P6_3$ ($\mathbf{a} = 2\mathbf{a}_p$, $\mathbf{b} = 2\mathbf{b}_p$, $\mathbf{c} = \mathbf{c}_p$) crystal structure reported for $BaAl_2O_4$ at room temperature has been carefully re-investigated by a combined transmission electron microscopy and neutron powder diffraction study. It is shown that the poor fit of this $P6_3$ ($\mathbf{a} = 2\mathbf{a}_p$, $\mathbf{b} = 2\mathbf{b}_p$, $\mathbf{c} = \mathbf{c}_p$) structure model for $BaAl_2O_4$ to neutron powder diffraction data is primarily due to the failure to take into account coherent scattering between different domains related by enantiomorphic twinning of the $P6_322$ parent sub-structure. Fast Fourier transformation of [0 0 1] lattice images from small localized real space regions (~10 nm in diameter) are used to show that the $P6_3$ ($\mathbf{a} = 2\mathbf{a}_p$, $\mathbf{b} = 2\mathbf{b}_p$, $\mathbf{c} = \mathbf{c}_p$) crystal structure reported for $BaAl_2O_4$ is not correct on the local scale. The correct local symmetry of the very small nano-domains is most likely orthorhombic or monoclinic.

1. Introduction

$BaAl_2O_4$ is a member of the large family of inherently flexible, stuffed tridymite tetrahedral framework structures [1–3]. It has been extensively investigated over recent times, partially as the result of an apparent paraelectric (PE) to improper ferroelectric (iFE) phase transition around 400 K [4–9] but also because of the fact that it is a promising luminescent host phase for new generation, long afterglow, luminescent materials [10–12].

The room temperature crystal structure of $BaAl_2O_4$ was first reported in 1937 [13] as refined from X-ray diffraction (XRD) data. It consists of corner-connected AlO_4 tetrahedra forming a tridymite related, tetrahedral framework sub-structure. The Ba ions are situated in the channels of this framework sub-structure (see Fig. 1b). Relative to their orientation in the ideal tridymite, $P6_3/mmc$, aristotype structure (see Fig. 1a), the constituent AlO_4 tetrahedra of $BaAl_2O_4$ are each rotated ~30° around the c-axis (compare Fig. 1a with Fig. 1b). This gives rise to a resultant parent structure space group symmetry of $P6_322$ with about the same unit cell dimensions as the ideal tridymite aristotype ($a_p = 5.209$ Å and $c_p = 8.761$ Å; the subscript p indicates this $P6_322$ average parent structure throughout the paper). Note that $P6_322$ is an enantiomorphic maximal subgroup of $P6_3/mmc$ and that the sense of the initial ~30° rotation of the tetrahedron around the c-direction (see Fig. 1a) can be in either a clockwise or an anti-clockwise direction (cf. the two orientational variants shown in Fig. 1b). This crystal structure for $BaAl_2O_4$ later appeared to be confirmed by early neutron diffraction work [14].

In the mean time, however, Hoppe and Schepers [15] had reported the observation of extra (satellite) reflections in powder XRD data implying a superstructure doubling of the $\mathbf{a}_p$ and $\mathbf{b}_p$ axes. This was subsequently confirmed via single-crystal XRD work [16,17]. While these additional satellite reflections were not used in their crystal structure refinement, Perrotta and Smith [17] nonetheless found that the O1 oxygen ion did not fall on the three-fold axis of the ideal $P6_322$ parent structure but rather was apparently disordered outside the three-fold axis (cf. Fig. 1c with Fig. 1b). This disordered oxygen ion position suggested that the superstructure doubling of the $\mathbf{a}_p$ and $\mathbf{b}_p$ axes might arise as the result of a collective pattern of tetrahedral tilting of the framework sub-structure around a basal plane rotation axis. Later still, single-crystal XRD data including the additional superstructure reflections was collected and the crystal structure refined in space group $P6_3$ ($a = 2a_p = 10.470$ Å and $c = c_p = 8.819$ Å) to $R = 12\%$ [18]. This resulted in a crystal structure (Fig. 2) where $\frac{3}{4}$ of the AlO_4 tetrahedra are significantly tilted around a basal plane axis (the orange tetrahedra of Fig. 2a) but $\frac{1}{4}$ of these tetrahedra (the green tetrahedra in Fig. 2a) are not. The local Al–O–Al bond angles along the c-direction (out of the page in Fig. 2a) are thus relaxed considerably to a far more crystal chemically reasonable value of 156° in the case of the orange tetrahedra (significantly less than 180° forced by the ideal $P6_322$ parent

* Corresponding author. Fax: +61 2 6125 4692.
E-mail address: ankie.larsson@anu.edu.au (A.-K. Larsson).

0022-4596/$ - see front matter © 2008 Elsevier Inc. All rights reserved.
doi:10.1016/j.jssc.2008.03.043

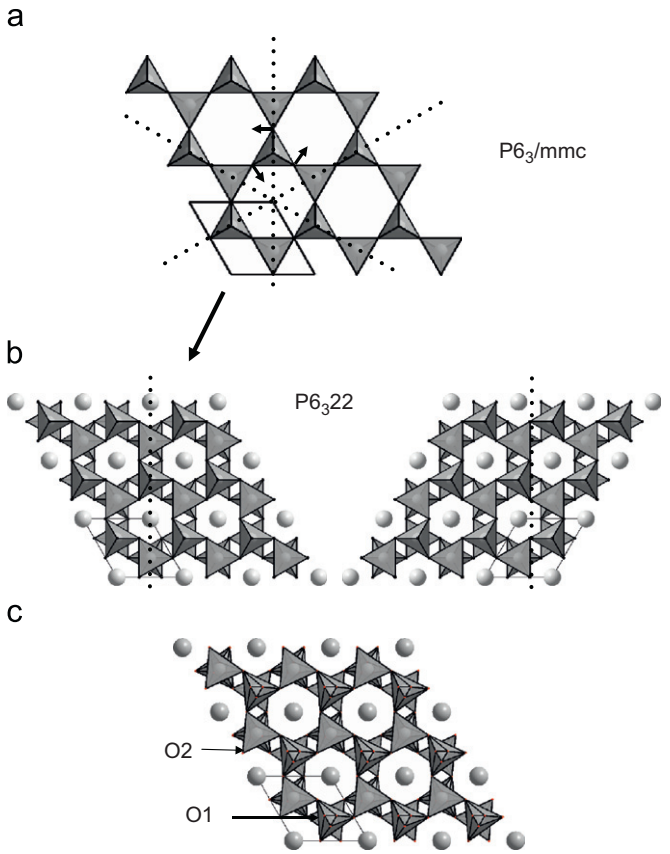

Fig. 1. (a) The average crystal structure of ideal $P6_3/mmc$ tridymite. The SiO_4 tetrahedra are corner linked and form large hexagonal open channels along the *c*-axis. The mirror planes are indicated together with arrows illustrating how these mirror planes are broken by rotations of tetrahedra. (b). The two enantiomorphs of the $P6_322$ $BaAl_2O_4$ structure in which the (AlO_4) tetrahedra are rotated 30° compared to tridymite. Ba atoms (grey spheres) are in the resulting triangularly distorted channels. (c) The split atom model of the average structure [17] in which the oxygen atoms are situated outside the triad axes and therefore indicate that locally the Al–O–Al bond angles along the *c*-axis is not 180° but considerably less.

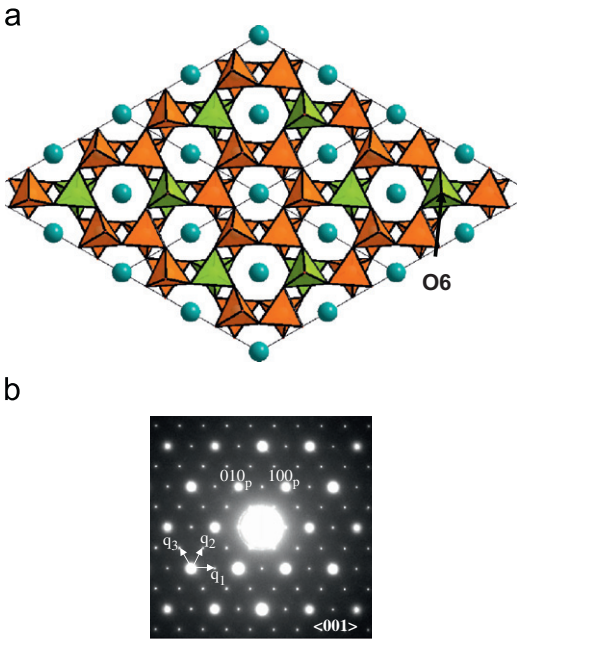

Fig. 2. (a) The reported crystal structure of $P6_3$ $BaAl_2O_4$ ($\mathbf{a} = 2\mathbf{a}_p$) [18]. (b) EDP recorded along the [001] zone axis of $BaAl_2O_4$. This EDP is compatible with the 3-**q** $P6_3$ $BaAl_2O_4$ ($\mathbf{a} = 2\mathbf{a}_p$) crystal structure resulting in the three symmetry equivalent modulation wave vectors $\mathbf{q}_1$, $\mathbf{q}_2$ and $\mathbf{q}_3$. Alternatively this reciprocal pattern would result from a twinned 1-**q** specimen (comp. Fig. 6b), where the modulation wave vector **q**, would take the different directions $\mathbf{q}_1$, $\mathbf{q}_2$ and $\mathbf{q}_3$ in different parts of the crystallite.

structure, see Fig. 1b) but constrained to remain at 180° in the case of the remaining $\frac{1}{4}$ of the tetrahedra (the green tetrahedra in Fig. 2b). Recently, a high-resolution electron microscopy (HREM) and electron diffraction (ED) study of $BaAl_2O_4$ was reported [4]. It found no evidence for any deviation from the reported $P6_3$ ($\mathbf{a} = 2\mathbf{a}_p$, $\mathbf{b} = 2\mathbf{b}_p$, $\mathbf{c} = \mathbf{c}_p$) structure [18].

While this $P6_3$ ($\mathbf{a} = 2\mathbf{a}_p$, $\mathbf{b} = 2\mathbf{b}_p$, $\mathbf{c} = \mathbf{c}_p$) crystal structure reported for $BaAl_2O_4$ is generally regarded as being well established, there have nonetheless been significant questions raised as to its validity. For example, during distance least square (DLS) modelling of the $Sr_{2-x}Ba_xAl_2O_4$ compound series, it was found that while the compositional and thermal expansion behaviour of the low *x* monoclinic members could be satisfactorily modelled, that of the high *x* 'hexagonal' members could not [3]. It was concluded that the problems encountered were largely due to space group symmetry constraints and that the reported structure and $P6_3$ space group symmetry may refer to an average structure only [3]. Likewise the existence of 180° Al–O–Al angles along the *c*-axis for $\frac{1}{4}$ of the tetrahedra also seems highly unlikely from the crystal chemical point of view (see e.g. Fig. 1 of [19]). Finally, it has recently been shown [20] that although crystal structure refinements of $BaAl_2O_4$ from synchrotron X-ray powder diffraction data give a very good fit using the $P6_3$ model [18], the fit to neutron powder diffraction data obtained using the same sample is quite poor. The implication is that the positions of the oxygen ions are not accurately described by the $P6_3$ ($\mathbf{a} = 2\mathbf{a}_p$, $\mathbf{b} = 2\mathbf{b}_p$, $\mathbf{c} = \mathbf{c}_p$) structure model [20].

The aim of the present investigation was to investigate the reasons for this poor fit of the $P6_3$ ($\mathbf{a} = 2\mathbf{a}_p$, $\mathbf{b} = 2\mathbf{b}_p$, $\mathbf{c} = \mathbf{c}_p$) structure model for $BaAl_2O_4$ to the neutron powder diffraction data. The main reason for this poor fit is shown to be coherent scattering between different domains related by enantiomorphic twinning of the $P6_322$ parent sub-structure as well as fine scale 180° rotation twinning and/or antiphase boundaries of the superstructure. In addition, direct evidence for broken hexagonal symmetry in the form of small nano-domains of an orthorhombic or monoclinic structure has been obtained using fast Fourier transforms (FFTs) of TEM lattice images. This suggests that the apparent $P6_3$ ($\mathbf{a} = 2\mathbf{a}_p$, $\mathbf{b} = 2\mathbf{b}_p$, $\mathbf{c} = \mathbf{c}_p$) hexagonal symmetry is caused by domain twinning on a very fine (and ill defined) scale. The superstructure can be refined either as the $P6_3$ ($\mathbf{a} = 2\mathbf{a}_p$) structure or, with slightly better residuals, a $P2_12_12_1$ structure and we discuss the underlying coherent scattering effects probably responsible for this.

2. Experimental

2.1. Sample preparation

The $BaAl_2O_4$ used in the TEM investigation was synthesized from $BaCO_3$ and Al_2O_3. Stoichiometric mixtures of the starting materials were ground together, calcined at 850 °C, reground, pressed to pellets and then reacted at 1400 °C for 2 h. The sample was then reground and heated at 1260 °C for 30 h before being annealed at 120 °C for a further 2 weeks. The sample used for neutron diffraction was synthesized by heating a stoichiometric mixture of $BaCO_3$ and Al_2O_3 at 850 °C for 16 h. The sample was then reground and reheated for four periods of 20 h at 1150 °C.

2.2. Data collection

The XRD data used to monitor the syntheses were collected using a Guinier-Hägg camera and a Shimadzu Lab X-6000 diffractometer with Bragg-Brentano geometry, both utilising Cu$K\alpha$ radiation. ED data were obtained using a Philips EM 430 transmission electron microscope (TEM) operating at 300 kV. Lattice images from crushed fragments were recorded using a Philips CM300T operated at 300 kV and equipped with a Gatan 694 slow-scan CCD camera. Powder neutron diffraction patterns were obtained using the high-resolution powder diffractometer (HRPD) at the high flux Australian reactor (HIFAR) facility, Australian Nuclear Science and Technology Organisation (ANSTO), Lucas Heights Science and Technology Centre [21]. Diffraction patterns were obtained at room temperature using a 20 g sample that was held in a 12 mm vanadium can. Data were collected using a wavelength of 1.884 Å from 5° to 150° (2θ angles) with a step size of 0.05° (2θ angle). The sample was rotated throughout the measurement to reduce the effects of preferred orientation.

3. Results

3.1. Refinement of powder neutron data in $P6_3$

The fit of a conventional crystal structure refinement of $BaAl_2O_4$ in space group $P6_3$ ($\mathbf{a} = 2\mathbf{a}_p$, $\mathbf{b} = 2\mathbf{b}_p$, $\mathbf{c} = \mathbf{c}_p$) [20] is shown in Fig. 3a. In this model (14 atoms, 29 structural parameters) and all other models, a single global displacement parameter and all variable coordinates are refined. Fig. 3b shows the difference plot and it is clear that the data are not well fitted.

Fig. 3c shows the difference plot from a refinement using only the $P6_322$ parent sub-structure (and the split atom model of $Ba_{0.6}Sr_{0.4}Al_2O_4$ [10], resulting in seven variable parameters). It is clear that this difference plot is quite similar to that obtained for the $P6_3$ superstructure refinement. This suggests strongly that the poor overall fit to the data is not because the satellite reflections are not well fitted but rather because the parent sub-structure is not well accounted for. From difference Fourier maps of the $P6_322$ parent sub-structure refinement, large peaks were found at (0.67,0,0) corresponding to the positions of the oxygen atoms of

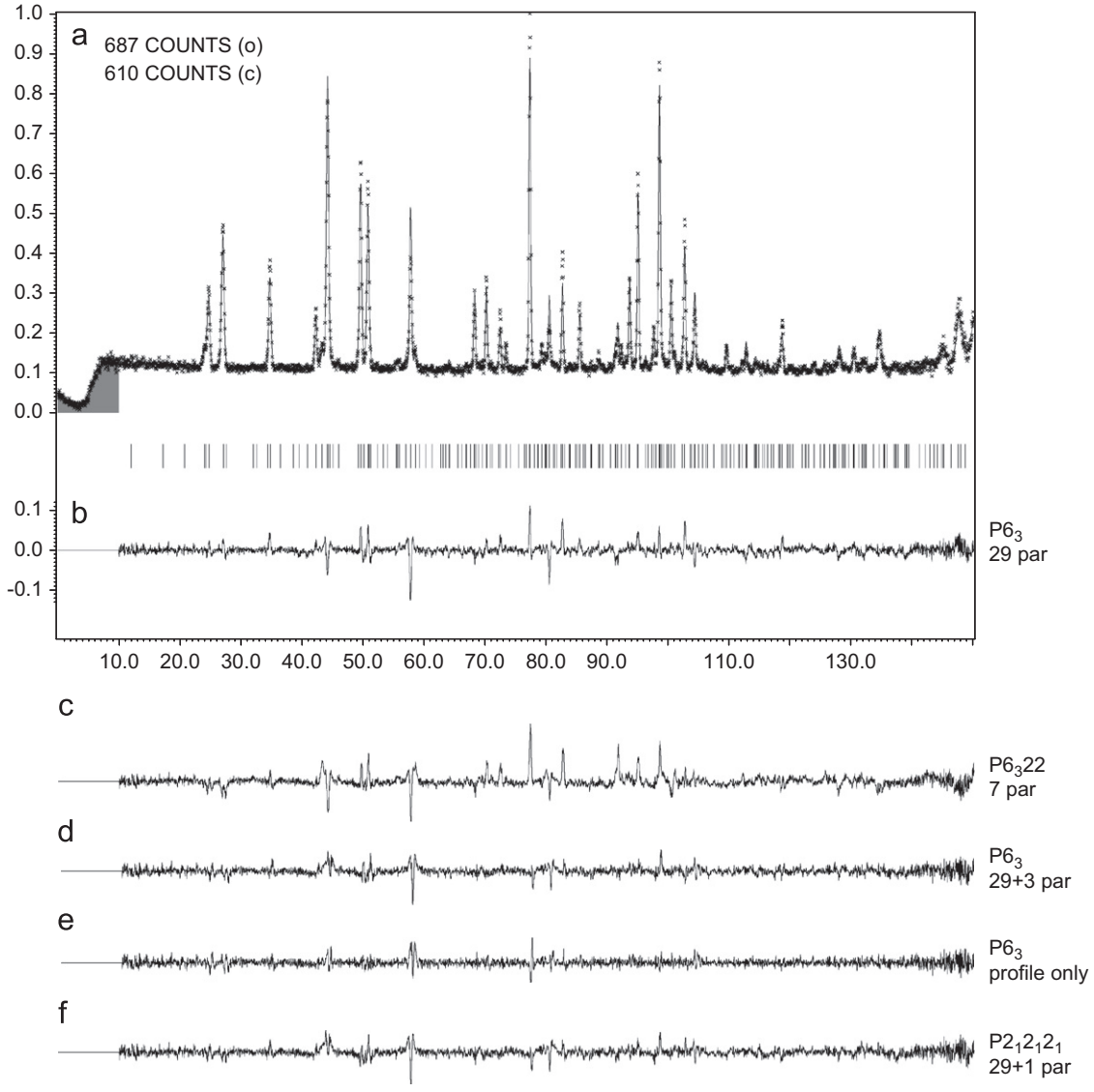

Fig. 3. (a) The neutron powder data profile fit for the $P6_3$ $BaAl_2O_4$ ($\mathbf{a} = 2\mathbf{a}_p$) model, (b–d) and (f) are difference plots for the different models while (e) is a profile fit only.

the superimposed second $P6_322$ enantiomorph shown in Fig. 1b. This could be interpreted as arising from rotational stacking fault disorder of the orientation of the tetrahedra. From Fig. 1, any such faulting would be expected to occur at the (001) planes. Electron diffraction patterns (EDPs) of $BaAl_2O_4$, however, never exhibit any diffuse streaking along the $\mathbf{c}_p^*$-axis that would be expected to accompany frequent such stacking faulting.

Considering that the $P6_322$ space group of the sub-structure is enantiomorphic (see Fig. 1b), and that the extra intensity in the difference Fourier maps coincides with the positions of the oxygen atoms of the superimposed second enantiomorph (cf. Fig. 1b), a model assuming a small portion of the second enantiomorph to scatter coherently with the bulk (first enantiomorphic) structure was then tested. This enantiomorphic twin model was simulated by adding a second set of atoms, related to the original set of atoms by reflection in a $(110)_p$ mirror plane of the original $P6_3$ structure model (see the dashed lines in Fig. 1a). This was achieved using the molecule option in JANA2006 [22]. All atoms in the asymmetric unit were transferred to a single molecule, and this molecule was then added in the additional position $(-y,-x,z)$. No parameters other than a collective occupancy factor (SOF) for this simulated enantiomeric twin were refined. With only this one extra parameter added to the refinement, the fit to the neutron data improved drastically. The occupancy of the second simulated twin refined to ~6%. We note that this refined value does not refer to the relative amounts of the two enantiomorphs present, but rather to coherent scattering effects that mainly depend on the coherence length of the neutron source relative to the domain size of the two enantiomorphs.

In an earlier TEM study, features interpreted as antiphase boundaries (see Fig. 5 in [4]) and 180° rotation twins (see Fig. 10 in [4]) associated with the presumed $P6_322$ ($\mathbf{a}_p$, $\mathbf{b}_p$, $\mathbf{c}_p$) to $P6_3$ ($2\mathbf{a}_p$, $2\mathbf{b}_p$, $\mathbf{c}_p$) PE to iFE phase transformation were imaged. DF (dark field) images using the parent $P6_322$ sub-structure reflections (see Fig. 10a of [4]) recorded perpendicular to the c-axis clearly showed 20–200 nm thick domains forming a banded microstructure strictly bounded by (001) planes. Much of this banded microstructure was reported to remain unaltered even at 1000 K, well above the transition temperature (400–670 K) to the parent $P6_322$ sub-structure [4]. They cannot therefore be assigned to antiphase boundaries or rotation twins associated with the $P6_3$ superstructure. At the time, this banded microstructure was assumed to be due to stacking faults. In light of the present crystal structure refinements, however, we suggest that these are actually images of the enantiomorphic twinning of the parent $P6_322$ sub-structure (see Fig. 1b).

The length scale (~20–200 nm) of this banded microstructure (i.e. of the enantiomorphic twinning) is much larger than the scale of the 180° rotation twin domains and the antiphase domains (10–50 nm). Consequently, the scattering between the 180° rotation twins and the antiphase domains should be coherent to a significantly larger extent than the scattering between the enantiomorphic twin domains. It then follows that it should be possible to improve the fit of the $P6_3$ ($2\mathbf{a}_p$, $2\mathbf{b}_p$, $\mathbf{c}_p$) model to the neutron data further by including the 180° rotation twins and the antiphase boundaries in the model.

The full set of possible antiphase boundaries, 180° rotation twins and enantiomeric twinning was therefore systematically introduced and evaluated. A list of some of the details of these refinements is shown in Table 1. The occupancy of all the 11 possible situations (added as molecules) cannot be independently refined. For instance, the occupancy of only one out of the three possible positions of the 'molecule' simulating the enantiomeric twin can be refined independently and we hence only use one of these positions (see Table 1). Likewise, the antiphase boundaries at position $(x+0.5,y+0.5,z)$ and the 180° rotation twin at position $(0.5-y,0.5-x,0.5-z)$ cannot be simultaneously refined. Only the 180° rotation twin was used in the final refinements. The best fit was found for a model in which the refined SOF = 6.8% for the molecule simulating the enantiomeric twin at $(0.5-y,0.5-x,z)$, SOF = 22.1% for a molecule simulating the 180° rotation twin at position $(0.5-y,0.5-x,0.5-z)$ and SOF = 14.4% for a molecule simulating an antiphase boundary at $(x+0.5,y,z)$. The resultant difference profile is shown in Fig. 3d. Note that the occupancy of the different molecules used to simulate the microstructure does not directly reflect the proportion of their respective corresponding domain volumes (with respect to the original set of atoms), but rather the size of the respective domains. Neither can these numbers be taken literally to determine exactly what antiphase and rotation twin boundaries are present as many of these would be strongly correlated in the refinements. We have simply (after careful evaluation) put the population of many of them to zero in order to find a simple model that best fits the neutron powder data (cf. Table 1).

The general conclusion from these refinements, that the refined proportion of the 180° rotation twins and antiphase boundaries are larger relative to the enantiomorphic twins, is totally compatible with the TEM images in [4] in which the scale

Table 1
Details of the residuals of the $P6_3$ refinements including the partially coherently scattering domains

Relationship to original "molecule"	Coordinates of new "molecule"	SOF	SOF	SOF	SOF
Enantiomorphic twin	$-y,-x,z$ $0.5-y,0.5-x,z$ $0.5-y,-x,z$ $0.5-y,0.5-x,z$		6.9		6.8
180 rot twin at ..2	$-y,-x,-z+1/2$ $0.5-y,-x,-z+1/2$ $0.5-y,0.5-x,-z+1/2$ $-y,0.5-x,-z+1/2$			32.1	22.1
Antiphase domains	$0.5+x,y,z$ $0.5+x,0.5+y,z$ $x,0.5+y,z$			17.7	14.4
R (all)		9.2	8.48		5.64
Rwp		7.53	6.82	6.39	5.89

Table 2
Coordinates for $BaAl_2O_4$ in the $P6_3$ model ($a = 10.4512(6)$ and $c = 8.7910(5)$ Å)

Atom	*Wyck* position	*x*	*y*	*z*	SOF
Ba1	2*a*	0.0000	0.0000	0.2500	1
Ba2	6*c*	0.507(2)	0.009(2)	0.253(8)	1
Al1	6*c*	0.163(6)	0.341(7)	0.056(1)	1
Al2	6*c*	0.152(6)	0.325(6)	0.45(1)	1
Al3	2*b*	0.3333	0.66667	0.95(1)	1
Al4	2*b*	0.3333	0.66667	0.56(1)	1
O1	6*c*	0.181(4)	0.000(3)	0.978(3)	1
O2	6*c*	0.690(2)	0.005(2)	0.058(3)	1
O3	6*c*	0.498(3)	0.181(3)	1.004(5)	1
O4	6*c*	0.175(3)	0.498(4)	0.993(4)	1
O5	6*c*	0.1161(8)	0.320(2)	0.255(4)	1
O6	6*c*	0.3333	0.6667	0.740(6)	1

In the refinements, the partially coherent scattering of the different enantiomorphs in the (001) banded microstructure as well as the 180° rotation twin and the antiphase boundaries was simulated by adding extra molecules of the original structure at the corresponding positions (see Table 1).

of the enantiomorphic twinning is on a significantly larger scale (20–200 nm compared to 10–50 nm).

The crystal structure model in space group $P6_3$ ($2\mathbf{a}_p$, $2\mathbf{b}_p$, $\mathbf{c}_p$) resulting from these refinements (Table 2) remains very similar to that which was previously refined [18,20] although the fit to the powder neutron data has improved drastically (cf. Figs. 3b and d). By comparing the difference profile of this final model (using one 180° rotation twin, one antiphase boundary and one enantiomorphic twin, Fig. 3d) with the pure profile fit (not using the intensities of the calculated structure, but only the positions of the peaks and the optimal intensities to fit to the data, Fig. 3e), it is clear that the data is now reasonably well fitted. The remaining major concern with this crystal structure is hence no longer the poor fit to the neutron data, but that the space group symmetry $P6_3$ does not allow relaxation of the 180° Al–O–Al angles along the *c*-axis for $\frac{1}{4}$ of the tetrahedra (the green tetrahedra in Fig. 2a). ED was therefore used in order to search for a lower symmetry.

3.2. Electron diffraction

Conventional selected area EDP's of $BaAl_2O_4$ (see e.g. Fig. 2b), taken from a relatively large area of diameter ~0.5 μm, were entirely consistent with the reported $P6_3$ ($\mathbf{a} = 2\mathbf{a}_p$, $\mathbf{b} = 2\mathbf{b}_p$, $\mathbf{c} = \mathbf{c}_p$; $\mathbf{a}^* = \frac{1}{2}\mathbf{a}_p^*$, $\mathbf{b}^* = \frac{1}{2}\mathbf{b}_p^*$, $\mathbf{c}^* = \mathbf{c}_p{}^*$) structure of Hörkner and Muller-Buschbaum [18]. As well as the strong Bragg reflections, **G**, of the underlying $P6_322$ parent structure, there are additional sharp, $\mathbf{G} \pm \frac{1}{2}\langle 1, -1, 0\rangle *$ satellite reflections. The three sets of symmetry equivalent commensurate modulations wave vectors giving rise to these additional satellite reflections are labelled $\mathbf{q}_1$, $\mathbf{q}_2$ and $\mathbf{q}_3$ respectively, in Fig. 2b. $P6_3$ space group symmetry requires that all three modulations simultaneously co-exist with the same amplitude in any one area of the specimen (i.e. $P6_3$ implies a so-called 3-**q** modulated structure).

A lower symmetry was tested for by moving the sample slightly relative to the electron beam, looking for systematic variations in relative intensities of the $\mathbf{G}\pm\mathbf{q}_1$, $\mathbf{G}\pm\mathbf{q}_2$ and $\mathbf{G}\pm\mathbf{q}_3$ satellite reflections. No such variations were detectable using conventional selected area ED. This is perhaps not surprising given that the area illuminated in order to take such an EDP is of diameter ~0.5 μm. Micro-diffraction (MD), involving a narrow beam condensed onto a much smaller illuminated area (in our case down to a diameter of ~30 nm) was thus also tried. Again, however, [0 0 1] MD patterns obtained always contained all three sets of satellite reflections $\mathbf{G}\pm\mathbf{q}_1$, $\mathbf{G}\pm\mathbf{q}_2$ and $\mathbf{G}\pm\mathbf{q}_3$ with similar intensities, i.e. no symmetry lower than $P6_3$ could be clearly detected by direct diffraction methods. Any local lowering of $P6_3$ space group symmetry must therefore involve twinning on the nano-scale. To further pursue this possibility, lattice imaging and FFT from a nano-scale local region was used.

3.3. Lattice images and fast Fourier transforms

Lattice images of $BaAl_2O_4$ were recorded along the $[0\,0\,1]_p$ zone axis (for a typical example, see Fig. 4a) and carefully investigated by calculating FFTs from localized nano-scale areas (see the circled regions in Fig. 4a) using the software programme CRISP [23]. FFTs of these circled areas (10 nm in diameter) are shown in Figs. 4b–d. The more intense, hexagonal set of reflections (circled in each case) correspond to the $\langle 1\,0\,0\rangle_p{}^*$ reflections of the $P6_322$ parent structure. These parent Bragg reflections, **G**, are again accompanied by satellite reflections in each of the FFTs, but clearly all three sets of $\mathbf{G}\pm\mathbf{q}_1$, $\mathbf{G}\pm\mathbf{q}_2$ and $\mathbf{G}\pm\mathbf{q}_3$ satellite reflections are not always simultaneously present. In Figs. 4b and d, for example, only one modulation wave vector ($\mathbf{q}_2$ in the case of Fig. 4b and $\mathbf{q}_1$ in the case of Fig. 4d) is present in each case. Note that the intensities of the circled parent $\langle 1\,0\,0\rangle_p{}^*$ Bragg reflections show-close-to-hexagonal symmetry in these FFT's (particularly in the case of Fig. 4d). Thus the presence of only one set of satellite reflections in the regions corresponding to Figs. 4b and d cannot reasonably be attributed to domain misorientation. In Fig. 4c, both $\mathbf{G}\pm\mathbf{q}_1$ as well as $\mathbf{G}\pm\mathbf{q}_2$ satellite reflections are present in the FFT (although the latter are significantly weaker than the former).

Such FFTs show that only one out of the star of the three, originally symmetry equivalent modulations characterized by the modulation wave vectors $\mathbf{q}_1$, $\mathbf{q}_2$ or $\mathbf{q}_3$, is locally present on the nano-scale. This means that $BaAl_2O_4$ locally has a 1-**q** modulated structure as opposed to a 3-**q** modulated structure. Hence the true local symmetry is not $P6_3$. The nano-scale domains, however, are so small (~10 nm) that there is significant overlap in thicker foil regions so that more than one modulation wave vector (of $\mathbf{q}_1$, $\mathbf{q}_2$ or $\mathbf{q}_3$) is often present in each FFT (see e.g. Fig. 4c). Nonetheless, large enough single-domain regions to produce a single-**q** FFT can easily be found from most lattice images.

In another case, sequential lattice images were recorded from one area. FFTs of some of these successive images shows that the

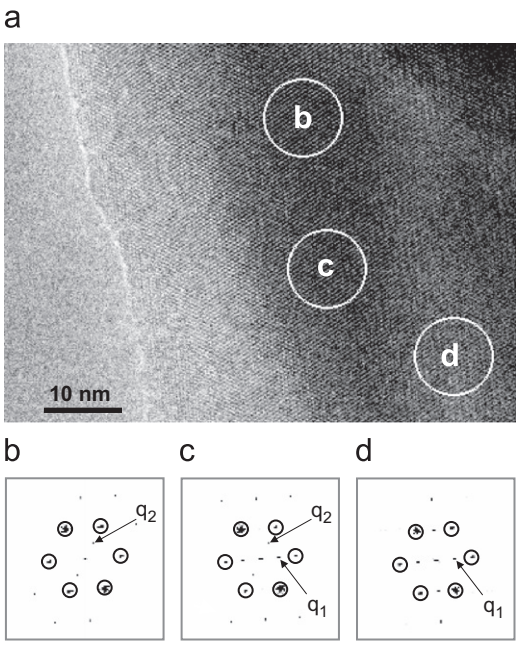

Fig. 4. (a) Lattice image of $BaAl_2O_4$. FFT of the marked areas are shown in (b)–(d).

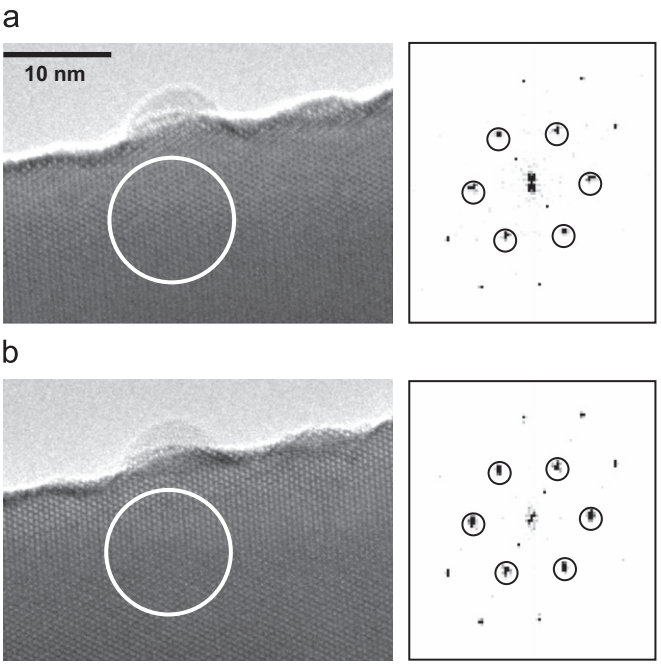

Fig. 5. (a and b) Two different lattice images of the same portion of a crystallite recorded with a few minutes difference. The FFTs of the circled portion of the crystallites shown to the right.

relative intensities of the three sets of $\mathbf{G}\pm\mathbf{q}_1$, $\mathbf{G}\pm\mathbf{q}_2$ and $\mathbf{G}\pm\mathbf{q}_3$ satellite reflections can sometimes vary from exposure to exposure. Figs. 5a and b, for example, were recorded from the same area of the same crystallite (again along the $[0\,0\,1]_p$ zone axis orientation). The two FFTs in Figs. 5b and d, taken from exactly the same area of the two images in Figs. 5a and c, show that the single-**q** modulation wave vector present has changed from $\mathbf{q}_1$ in Fig. 5b to $\mathbf{q}_2$ in Fig. 5d. Note that the exact tilt orientation of the two successive images is virtually identical as is clear from the relative intensities of the parent Bragg reflections. This suggests that the essentially static nano-domain twin boundaries can move under the influence of the electron beam. This observation is consistent with earlier TEM observations [4] showing that antiphase domain boundaries in $BaAl_2O_4$ can become mobile under the influence of the electron beam.

3.4. Symmetry considerations

If the reported hexagonal $P6_3$, 3-**q** structure model for $BaAl_2O_4$ is not correct, the question becomes what other 1-**q** structural models are possible and what is the appropriate local space group symmetry? One possibility is provided by the low temperature, monoclinic $P2_1$ structure of $SrAl_2O_4$ [24] shown in Fig. 6a. The reciprocal lattice nodes of this $P2_1$ superstructure phase can be described as $\mathbf{H}=\mathbf{G}+\mathbf{q}_1$, where **G** is the set of Bragg reflections of the $P6_322$ parent structure and $\mathbf{q}_1=\mathbf{b_m}^*=\frac{1}{2}[1,-1,0]_p^*$ is the

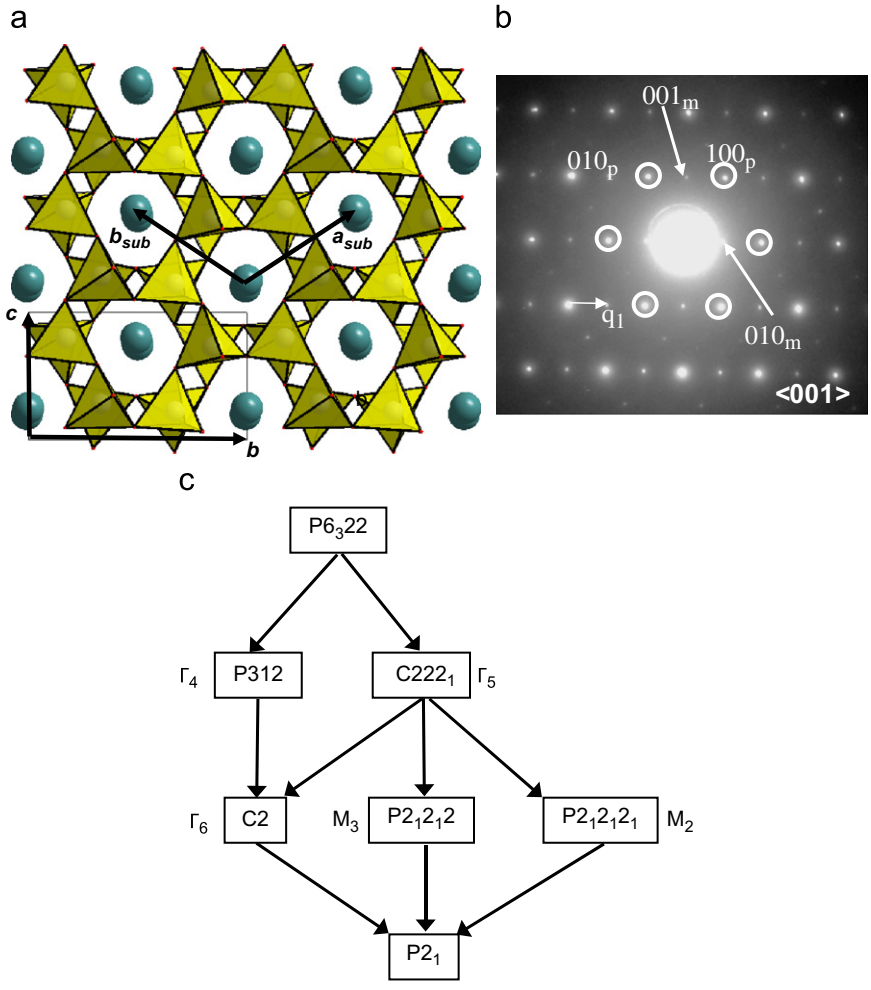

Fig. 6. (a) The $P2_1$ $SrAl_2O_4$ crystal structure. (b) The corresponding EDP is indexed in the $P6_322$ parent as well as in the $P2_1$ superstructure cell. (c) The group–subgroup relationship between the $P6_322$ parent and the $P2_1$ superstructure.

single-**q**, commensurate modulation wave vector. The reciprocal lattice of this $P2_1$, $SrAl_2O_4$ structure is hence compatible with the local 1-**q** structure of $BaAl_2O_4$ detected above via FFT's of lattice images. Given the reported miscibility between $SrAl_2O_4$ and $BaAl_2O_4$ [1], the symmetry modes of distortion of this 1-**q**, $P2_1$ structure of $SrAl_2O_4$ were explored. The real space relation between the supercell ($a = 8.447$ Å, $b = 8.881$ Å, $c = 5.163$ Å and $\beta = 93.4^\circ$) and the average $P6_322$ parent cell is $\mathbf{a} = \mathbf{c}_p$, $\mathbf{b} = \mathbf{a}_p - \mathbf{b}_p$ and $\mathbf{c} = \mathbf{a}_p + \mathbf{b}_p$. The relationship in reciprocal space is then $\mathbf{a}^* = \mathbf{c}_p^*$, $\mathbf{b}^* = \frac{1}{2}(\mathbf{a}_p^* - \mathbf{b}_p^*)$ and $\mathbf{c}^* = \frac{1}{2}(\mathbf{a}_p^* + \mathbf{b}_p^*)$ (see Fig. 6b). The group–subgroup lattice showing the relationship between the parent $P6_322$ sub-structure and the resultant $P2_1$ room temperature structure of $SrAl_2O_4$ is shown in Fig. 6c, as obtained using the Bilbao Crystallographic Server [25,26]. The symmetry of the modes (irreducible representations) yielding the different intermediate symmetries is indicated in Fig. 6c. There is no symmetry breaking normal mode, which can produce the observed $P2_1$ symmetry directly. In fact, if the experimental $P2_1$ structure of $SrAl_2O_4$ is decomposed into the different symmetry modes indicated in Fig. 6c, the distortions M_2 and Γ_6 with isotropy subgroups $P2_12_12_1$ and $C2$, respectively, are dominant, both having similar amplitudes. $P2_1$ space group symmetry is only obtained when the two distortion modes superpose. This justifies the reasonable suggestion by Rodehurst et al. [2] of an intermediate phase of $C2$ symmetry corresponding to the freezing in of the Γ_6 primary order parameter, provided (as is usually the case) that the M_2 and Γ_6 modes do not condense out simultaneously. The dominant M_2 and Γ_6 distortion modes of $SrAl_2O_4$ can be described as essentially rigid unit modes (RUMs) of the corner-connected Al_2O_4 tetrahedral framework coupled with correlated displacements of the Ba atoms. The two modes introduce correlated rotations of the AlO_4 tetrahedra (around the $[1,2,0]_p$ axis in the case of the M_2 mode, and around the $[1,0,0]_p$ axis in the case of the Γ_6 mode), that separately are able to relax the unfavourable 180° Al–O–Al angles present in the average $P6_322$ parent structure.

The M_2 mode is three-fold degenerate and could, in principle, be associated with a three-dimensional order parameter. In general, three distortion waves associated with the three symmetry related modulation wave vectors $\mathbf{q}_1$, $\mathbf{q}_2$ and $\mathbf{q}_3$ (see Fig. 2b) can superpose within an M_2 distortion, the three of them satisfying the same RUM properties. The $P2_12_12_1$ distortion, realized in $SrAl_2O_4$, corresponds to the particular case where only one of these three modulation waves is present in the overall distortion. Alternatively, if the three distorting modes superpose coherently with the same amplitude, the resulting symmetry would be $P6_3$ with $\mathbf{a} = 2\mathbf{a}_p$ [8,27]. The reported $P6_3$ ($2\mathbf{a}_p$,$2\mathbf{b}_p$,$\mathbf{c}_p$) $BaAl_2O_4$ structure is consistent with this scenario. The larger size of Ba compared with Sr tends to stabilize the parent $P6_322$ sub-structure, reducing the RUM instabilities of the framework. The Γ_6 distortion might then disappear, leaving the M_2 mode with a much reduced amplitude. If the remaining M_2 mode changed its direction to become a 3**q** distortion, instead of the 1**q** distortion observed in $SrAl_2O_4$, $P6_3$ symmetry would result. Such a $P6_3$ structure would be polar, and the phase would be an iFE with an induced secondary polarization along the hexagonal axis. The observation of small spontaneous polarizations in ceramic samples of $BaAl_2O_4$ has been explained within this context [6–8].

As observed in the above lattice images and their corresponding FFTs, however, the local crystal structure is clearly single-**q**, although the single-**q** domain regions are rather small (~10 nm) and do not produce any noticeable strain in the hexagonal sublattice. This suggests significant coherence between the nano-twinned regions which may be compatible with the relatively successful crystal structure refinements in the apparent average $P6_3$ ($2\mathbf{a}_p$,$2\mathbf{b}_p$,$\mathbf{c}_p$) unit cell. As a test, crystal structure refinements were also performed in the single-**q**, $P2_12_12_1$ space group (allowing a single-**q**, M_2 distortion mode) as well as in a $P2_1$ space group symmetry (allowing an additional Γ_6 distortion mode).

3.5. Refinement of powder neutron data in $P2_12_12_1$ and $P2_1$

In order to simplify the single-**q** models, only the microstructure associated with the enantiomorphic twinning of the $P6_322$ parent sub-structure was simulated in what follows. No attempt to simulate the fine scale 120° rotation twinning was made.

There were no indications in the power neutron data for any deviation from the metrically hexagonal symmetry, i.e. the pure profile fit was not significantly improved by allowing metric distortions of the hexagonal lattice. For the first attempt at a single-**q** crystal structure refinement, the $SrAl_2O_4$ coordinates [24] were used as a starting point. The structure was refined in space group $P2_1$ allowing the presence of both M_2 and Γ_6 distortion modes. The crystal structure refinements converged to a reasonable crystal structure. The unrestrained tetrahedral distances were all reasonable ($1.63 < d_{Al-O} < 1.88$ Å) although the refinements needed to be dampened (0.1) to be stable. The resulting difference plot, however, was very similar to the difference plot from the original $P6_3$ ($2\mathbf{a}_p$,$2\mathbf{b}_p$,$\mathbf{c}_p$) refinement.

We then tried a $BaAl_2O_4$ structure model refinement using the space group symmetry $P2_12_12_1$, thereby excluding the possibility of a Γ_6 distortion mode and leaving only a single-**q**, M_2 distortion mode. The fit of this model to the neutron data was significantly better than that achieved for the $P2_1$ model despite the much smaller number of refined parameters (7 atoms, 23 parameters, $R_{all}/R_p = 7.69/6.86$). The fit was improved further when the oxygen atoms were split into two positions. This model was found assuming distortions away from $P2_12_12_1$ towards the $P2_1$ structure model. In this model, all coordinates except those corresponding to the largest amplitudes of the Γ_6 distortion mode decomposed from the $SrAl_2O_4$ structure (cf. Fig. 6c) were restrained for each oxygen pair so that only four additional parameters, y[O1s] and x[O2s–O4s] were introduced. It was found that if in addition, z[O1s] was allowed to vary independently from z[O1], the residuals reduced further. The resultant structure (11 atoms, 29 parameters, $R_{all}/R_p = 5.10/5.95$) had somewhat better Bragg residuals than the $P6_3$ ($\mathbf{a} = 2\mathbf{a}_p$) $BaAl_2O_4$ model and a virtually identical profile fit. Hence the two very different models in $P2_12_12_1$ and in $P6_3$ ($2\mathbf{a}_p$, $2\mathbf{b}_p$, $\mathbf{c}_p$) fit equally well to the

Table 3
Coordinates for $BaAl_2O_4$ in the $P2_12_12_1$ model ($a = 8.7913(6)$, $b = 9.051(1)$ and $c = 5.2256(6)$ Å)

Atom	*Wyck* position	*x*	*y*	*z*	SOF
Ba	4*a*	0.504(2)	0.244(2)	0.504(2)	1
Al1	4*a*	0.301(2)	0.923(4)	0.494(6)	1
Al2	4*a*	0.308(2)	0.411(3)	0.025(5)	1
O1	4*a*	0.504(2)	0.899(4)	0.464(5)	0.5
O1s	4*a*	0.504	0.942(4)	0.409(4)	0.5
O2	4*a*	0.262(4)	0.250(2)	0.133(5)	0.5
O2s	4*a*	0.212(6)	0.250	0.133	0.5
O3	4*a*	0.250(5)	0.435(2)	0.676(4)	0.5
O3s	4*a*	0.293(4)	0.435	0.676	0.5
O4	4*a*	0.287(4)	0.076(2)	0.683(3)	0.5
O4s	4*a*	0.250(6)	0.076	0.683	0.5

The oxygen atoms are split into two positions assumed to be statistically occupied (50% in each). O1 is split only along *x*, while O2–O4 are split only along y (which is compatible with a local $P2_1$ $SrAl_2O_4$-type structure). In the refinements, the partially coherent scattering of the different enantiomophs in the banded microstructure was simulated by adding atomic positions corresponding to the second enantiomer (at *x*, *y* and $-z$) with the refined collective (apparent) SOF of 6.8%.

neutron powder data (compare Figs. 3d and f). The structural details for the final refinements are listed in Tables 2 and 3.

4. Discussion and conclusions

The above refinements show that both enantiomorphs of the $P6_322$ parent sub-structure are present in coherently scattering portions of the sample. This not only explains the large residuals in difference plots of earlier published neutron powder refinements, but it also reveals the structural origin of the banded microstructure in TEM images of $BaAl_2O_4$ published in [4]. Images recorded perpendicular to the *c*-axis clearly showed that 20–100 nm thick domains form a (001) banded microstructure. The domains were hardly visible in bright field (BF) images, but obvious in dark field (DF) images using the parent $P6_322$ sub-structure reflections. Using an *in situ* heating stage, the same authors also showed that some of these features disappeared on increasing the temperature while others remained unaltered even at 1000 K, well above the transition temperature to the parent $P6_322$ sub-structure [4]. The previous interpretation [4] was that the bands that disappeared at the transition temperature (at 450 K) were probably due to twinning while those persisting above 1000 K were assumed to be stacking faults. In light of the present crystal structure refinements it can now be reinterpreted that the domains surviving the phase transition are due to twinning of the *parent sub-structure*, resulting in a mixture of the two enantiomorphs. The domains that disappear at the phase transition can be assumed to consist of antiphase boundaries and/or domain borders between differently oriented domains.

When this enantiomorphic twinning of the sub-structure is taken into account in the refinements, residuals in the difference plot appear smaller for the $P6_3$ ($2\mathbf{a}_p$,$2\mathbf{b}_p$,$\mathbf{c}_p$), $BaAl_2O_4$ model. However, as we also had detected the existence of nano-domains in which only one of the star of symmetry equivalent vectors $\mathbf{q}_1$, $\mathbf{q}_2$ and $\mathbf{q}_3$ was present and this is not compatible with the $P6_3$ $BaAl_2O_4$ ($\mathbf{a} = 2\mathbf{a}_p$) structure, models using the (1-$\mathbf{q}$) $P2_1$ $SrAl_2O_4$-type structure as a starting point were also refined. The best of these models was found to be a model in $P2_12_12_1$, a minimal super group of $P2_1$, in which the oxygens were split into two atoms.

In summary, the superstructure can be refined reasonably well in both the $P6_3$ (3$\mathbf{q}$) and the $P2_12_12_1$ (1$\mathbf{q}$) space groups. We conclude that both descriptions can be considered valid, and that they represent different interpretation of scattering from small partially coherently scattering domains. The $P6_3$ model reflects the overall symmetry of bulk crystals, even on the microscopic scale, while the $P2_12_12_1$ model reflects that the local symmetry is lower, possibly even monoclinic. Regardless of the symmetry used, neighbouring domains will at least partially scatter coherently and affect the crystal structure refinement with respect to the true local atomic positions. In addition, a significant portion of the crystal (i.e. antiphase boundaries and twin boundaries) has local arrangements of the atoms, which deviate from that inside a single domain.

At this stage, details are not quite clear regarding the apparent discrepancy between our observation of single-$\mathbf{q}$ domains and the earlier microstructural observations reported in [4] which were interpreted in terms of a local $P6_3$ structure model. FFTs performed directly on published images from this earlier work (i.e. Fig. 6 of [4]) show that single-$\mathbf{q}$ regions also exist in these images. In our TEM investigations we could not image the APBs as clearly as in the earlier HREM work [4]. On the other hand, it was observed both in this work and in the earlier HREM work that the domain boundaries can become mobile with beam heating. This provides a potential explanation for the slightly different images recorded with different microscopes, as this behaviour would be sensitive to the voltage and other operating conditions. In addition, a kink in the temperature dependence of unit cell parameters has been reported at 300 K [9] providing the possibility that two very similar phases might be stable very close to room temperature. Thus the possibility of both a 1$\mathbf{q}$ and a 3$\mathbf{q}$ phase cannot be excluded. Further HREM studies using a cold stage will be needed in order to understand more details of the local symmetry and the nature of the microstructure.

In order to get further insight into the theoretical stability of the different possible local symmetries of $BaAl_2O_4$, *ab-initio* and bond valence calculations have been initiated.

Acknowledgement

Financial support from the Australian Research Council is gratefully acknowledged.

References

[1] C.M.B. Henderson, D. Taylor, Mineral. Mag. 45 (1982) 111–127.
[2] U. Rodehorst, M.A. Carpenter, S. Marion, M.B. Henderson, Mineral. Mag. 67 (5) (2003) 989–1013.
[3] D. Taylor, M.J. Dempsey, C.M.B. Henderson, Bull. Mineral. 108 (1985) 643–652.
[4] A.M. Abakumov, O.I. Lebedev, L. Nistor, G. Van Tendeloo, S. Amelinckx, Phase Transit. 71 (2000) 143–160.
[5] A.A. Bush, A.G. Laptev, Sov. Phys. Solid State 31 (1989) 535–536.
[6] S.-Y. Huang, R. Von der Muell, J. Ravez, J.P. Chaminade, P. Hagenmuller, M. Couzi, J. Solid State Chem. 109 (1994) 97–105.
[7] S.-Y. Huang, R. von der Muell, J. Ravez, M. Couzi, Ferroelectrics 159 (1994) 127–132.
[8] H.T. Stokes, C. Sadate, M. Hatch, L.L. Boyer, M.J. Mehl, Phys. Rev. B 65 (2002) 1–4, 064105.
[9] V.V. Zhurov, A.A. Bush, S.A. Ivanov, S.Y. Stefanovich, B.N. Romanov, Sov. Phys. Solid State 33 (1991) 960–963.
[10] K. Fukuda, T. Iwata, T. Orito, J. Solid State Chem. 178 (2005) 3662–3666.
[11] Y. Lin, Z. Zhang, Z. Tang, J. Zhang, Z. Zheng, X. Lu, Mater. Chem. Phys. 70 (2001) 156–159.
[12] H. Takasaki, S. Tanabe, T. Hanada, J. Ceram. Soc. Japan 104 (1996) 322–326.
[13] S. Wallmark, A. Westgren, Ark. Kemi, Mineral. Geol. B 12 (1937) 1–4.
[14] C. Do Dinh, C. Bertaut, Bull. Soc. Franc. Mineral. Cristallogr. 88 (1965) 413–416.
[15] R. Hoppe, B. Schepers, Naturwissenschaftern 47 (1960) 376.
[16] R.H. Arlett, J.G. White, M. Robbins, Acta Crystallogr. 22 (1967) 315.
[17] A.J. Perrotta, J.V. Smith, Bull. Soc. Franc. Mineral. Cristallogr. 91 (1968) 85–87.
[18] V.W. Horkner, H. Muller-Buschbaum, Z. Anorg. Allg. Chem. 451 (1979) 40–44.
[19] W. Depmeier, in: H. Karge, J. Weitkamp (Eds.), Structures and Structure Determination, vol. 2, Springer, 1999.
[20] P.J. Saines, M.M. Elcombe, B.J. Kennedy, J. Solid State Chem. 179 (2006) 613–622.
[21] C.J. Howard, C.J. Ball, M.M. Davis, M.M. Elcombe, Aust. J. Phys. 36 (1983) 507–518.
[22] V. Petricek, M. Dusek, L. Palatinus, Crystallographic Computing System, Institute of Physics, Praha, Czech Republic, 2006.
[23] P. Oleynikov, CRISP, 2003.
[24] A.-R. Schulze, H. Muller-Buschbaum, J. Anorg. Allg. Chem. 475 (1981) 205–210.
[25] M.I. Aroyo, A. Kirov, C. Capillas, J.M. Perez-Mato, H. Wondratscheck, Acta Crystallogr. A 62 (2006) 115–128.
[26] M.I. Aroyo, J.M. Perez-Mato, C. Capillas, E. Kroumova, S. Ivantchev, G. Madariaga, A. Kirov, H. Wondratscheck, Z. Kristallogr. 221 (1) (2006) 15–27.
[27] H.T. Stokes, D.M. Hatch, B.J. Campbell, ISOTROPY, stokes.byu.edu/isotropy.html, 2007.